

Analysis of the dissipative range of the energy spectrum in grid turbulence and in direct numerical simulations

Anastasiia Gorbunova^{1,2}, Guillaume Balarac^{2,4}, Mickaël Bourgoïn³, Léonie Canet^{1,4},
Nicolas Mordant² and Vincent Rossetto¹

¹Université Grenoble Alpes, Centre National de la Recherche Scientifique, LPMMC, 38000 Grenoble, France

²Université Grenoble Alpes, Centre National de la Recherche Scientifique, LEGI, 38000 Grenoble, France

³ENS Lyon and Centre National de la Recherche Scientifique, Physics Department, 69000 Lyon, France

⁴Institut Universitaire de France, 1 rue Descartes, 75231 Paris, France



(Received 6 September 2019; accepted 24 March 2020; published 29 April 2020)

We present a statistical analysis of the behavior of the kinetic-energy spectrum in the dissipative range of fully developed three-dimensional turbulence, with the aim of testing a recent prediction obtained from the nonperturbative renormalization group. Analyzing spectra recorded in experiments of grid turbulence, generated in the Modane wind tunnel, and spectra obtained from high-resolution direct numerical simulations (DNSs) of the forced Navier-Stokes equation, we observe that the spectra decay as a stretched exponential in the dissipative range. The theory predicts a stretching exponent $\alpha = 2/3$, and the data analyses of the numerical and experimental spectra are in close agreement with this value. This result also corroborates previous DNS studies which found that the spectrum in the near-dissipative range is best modeled by a stretched exponential with $\alpha < 1$.

DOI: [10.1103/PhysRevFluids.5.044604](https://doi.org/10.1103/PhysRevFluids.5.044604)

I. INTRODUCTION

The very chaotic nature of the motion of a fluid driven to a turbulent state calls for a statistical description. A striking feature of three-dimensional turbulence is the emergence of very robust universal statistical properties, such as the well-known $k^{-5/3}$ decay of the energy spectrum over a wide range of length scales called the inertial range. This inertial range exists at sufficiently high Reynolds numbers, when the typical scale at which energy is injected (called the integral scale L) and the microscopic scale (called the Kolmogorov scale η) at which it is dissipated by molecular friction are well separated.

The first understanding of these properties was provided by the pioneering statistical theory of turbulence proposed by Kolmogorov, and referred to as K41 [1–4]. K41 theory relies on the fundamental assumptions that the small-scale turbulence is statistically independent of the large scales; that it is locally homogeneous, isotropic, and steady; and that the average energy dissipation rate per unit mass ϵ is finite and independent of the kinematic viscosity ν in the limit $\nu \rightarrow 0$. This implies that the statistical properties of small-scale turbulence should be determined uniquely by ϵ and ν . In particular, the energy spectrum should take the universal form

$$E(k) = \epsilon^{2/3} k^{-5/3} f(k\eta) \quad (1)$$

where $\eta = \nu^{3/4} \epsilon^{-1/4}$ is the Kolmogorov length scale. The function f is universal. In the inertial range, viscous effects are expected to be negligible, so that the spectrum should not depend on η , which implies that $f(x)$ should tend to a constant C_K for $x \rightarrow 0$, while f should quickly decay at large wave numbers $x \gtrsim 1$, which corresponds to the dissipative regime [5].

Although f is expected to be universal, its analytical expression is not known. Several early empirical expressions of the form $f(x) \sim x^{-\beta} \exp(-\mu x^\alpha)$, with different values for α (1/2 [6], 3/2

[7], $4/3$ [8], or 2 [9–11]), were proposed, on the basis of approximate fits of experimental data or (approximate) analytical considerations [12]. Also, different theoretical arguments focusing on the limit of large k (direct interaction approximation [5], asymptotic expansions [13–15]) advocated that in this limit, i.e., sufficiently deep in the far-dissipative range, the spectrum should decay as a pure exponential $\alpha = 1$. Alternatively, the multifractal formalism predicts a universal form of the spectrum involving the Reynolds number [16].

Subsequently, the behavior of the spectrum in the dissipative range has been extensively studied in experiments [17–20] and direct numerical simulation (DNS) [21–27]. Accurate experimental measurements of the spectrum at small scales are difficult to obtain, and several fits of the spectrum in the dissipative range have been proposed, for instance, pure exponential functions with $\alpha = 1$ but on two successive separate ranges in [17], or a single pure exponential but with different coefficients μ in [20,28]. Conversely, the analysis of [18] concluded that an exponential with $\alpha = 2$ was the best fit for the experimental data, while still another empirical form is proposed in [29].

The DNS can in principle provide more accurate data for the spectrum in the dissipative range, but their high computational cost limits the studies to either low or moderate Reynolds numbers in order to reach high spectral resolution [22,23,25,27] or to lower spectral resolutions to reach higher Reynolds numbers [21,24,26]. In practice, most of these works assumed that $\alpha = 1$, and aimed at determining the exponent β for the power laws (or combination of power laws) in front and the value of μ . Although a pure exponential fit was shown to be a reliable model for the spectrum at very low Reynolds numbers [27], it turned out not to be suitable to model the whole dissipative range already at moderate Reynolds numbers [23], and the result of the fit was found to depend significantly on the choice of the fitting range [24].

An extended analysis of the existing results for the dissipative range is provided in a recent account [30]. This paper (and previous studies) points to the conclusion that there exist two distinct regimes: the near-dissipative range (NDR) for $0.2 \lesssim k\eta \lesssim 4$ and the far-dissipative range (FDR) for $k\eta \gtrsim 4$. In the NDR, the logarithmic derivative of the spectrum is not linear, such that a pure exponential is not a consistent description, and its curvature indicates that $\alpha < 1$. In the FDR, the decay of the spectrum is well described by an exponential ($\alpha = 1$). This finding explains the failure of previous attempts to describe the whole dissipative range as a pure exponential with various power laws. The authors of [30] proposed a phenomenological modeling as a superposition of two exponentials, one with $\alpha < 1$ dominating in the NDR and one with $\alpha > 1$ dominating in the FDR. Note that no consensus seems to be reached concerning the power laws multiplying the exponentials in either regime.

Independently, a theoretical prediction for the behavior of the spectrum in the dissipative range has been recently obtained from a nonperturbative renormalization-group (NPRG) approach. This theoretical approach is a “first-principles” one, in the sense that it is based on the Navier-Stokes (NS) equation, without involving any phenomenological inputs or uncontrolled approximations. It has recently led to progress in the understanding of homogeneous isotropic and stationary turbulence, by providing the time dependence of multipoint correlation functions in the turbulent state [31,32]. Concerning the energy spectrum, the NPRG yields a stretched exponential behavior with $\alpha = 2/3$ in the NDR, and a regular one (pure exponential) in the FDR. This prediction provides a theoretical justification for the two-exponential phenomenological model proposed in [30]. This value for α in the NDR was then confirmed in DNS [33], and also in experiments of von Kármán turbulent swirling flow [34]. However, obtaining a quantitative estimate of the exponent of the stretched exponential is a difficult task, as it requires a sufficiently extended dissipative range and a high resolution.

In this paper, we perform DNS with a different compromise compared to previous studies favoring higher Reynolds numbers while keeping a sufficient spectral resolution in the NDR in order to reliably probe this regime. Moreover, we present a statistical analysis of the experimental data recorded in the Modane wind tunnel, featuring grid turbulence. Grid turbulence appears as a particularly suitable setup to investigate the dissipative range, since high Reynolds numbers can be attained, and the Kolmogorov scale is typically larger in the air than in liquids, such that a higher resolution can be expected. Also, the unique dimensions of the S1MA wind tunnel of ONERA in

Modane, where the experiments discussed here were performed, allow one to investigate relatively high Reynolds number regimes with yet experimentally well-resolved dissipative scales [35]. In the following, we focus on the NDR, and more specifically on the exponential part, irrespective of the power laws. We find from our analysis that the energy spectrum follows the predicted stretched exponential behavior, with an estimated exponent $\alpha = 0.68 \pm 0.19$, in close agreement with the NPRG result.

The remainder of the paper is organized as follows. In Sec. II, we give some details on the NPRG prediction. We present in Sec. III the results from the DNS, and in Sec. IV the statistical analysis of the experimental data. Additional details are reported in the Appendix.

II. THEORETICAL PREDICTIONS FROM THE NONPERTURBATIVE RENORMALIZATION GROUP

We present in this section the principle of the NPRG and the main ideas underlying the derivation of Eq. (6) for the spectrum in the dissipative range, which we aim at testing. The purpose of this section is not to give technical details on its derivation, which can be found in [31,33], but rather to emphasize the underlying assumptions: it is based on the stochastic Navier-Stokes equation, and on an expansion at large wave numbers, the leading term of which can be calculated exactly without any further approximations. One may resume directly at Eq. (4) for the result relevant for this paper.

The idea of applying the renormalization group (RG) to turbulence [36–40] originates in the observation that the statistical properties of a turbulent flow are universal and described by power laws in the inertial range. These power laws are the hallmarks of scale invariance. The source of scale invariance at a critical point is the emergence of fluctuations at all scales. The RG, as originally conceived by Wilson [41], is a method to efficiently average over these (non-Gaussian) fluctuations to obtain the critical properties of the system. It should thus provide a valuable tool to study fully developed turbulence, which intrinsically involves length scales over many orders of magnitude.

The NPRG is a modern formulation, both functional and nonperturbative, of the Wilsonian RG, which turned out to be powerful to compute the properties of strongly correlated systems in high-energy physics, condensed matter, and statistical physics [42–44]. It is only recently that turbulence has been revisited using functional and nonperturbative approaches [31,32,45–47]. Exact results were obtained in this framework for the time dependence of multipoint correlation functions of the stationary turbulent flow in the limit of large wave numbers [31,32]. These results hence pave the way towards a deeper understanding of the fundamental properties of turbulence.

The starting point is the forced NS equation for incompressible flows

$$\partial_i \vec{v} + \vec{v} \cdot \vec{\nabla} \vec{v} = -\frac{1}{\rho} \vec{\nabla} p + \nu \nabla^2 \vec{v} + \vec{f}, \quad \vec{\nabla} \cdot \vec{v} = 0 \quad (2)$$

where ν is the kinematic viscosity and ρ is the density of the fluid. We are interested in universal properties of turbulence. These properties are expected not to depend in particular on the precise form of the forcing mechanism. We hence consider, as is common in field-theoretical approaches [39], a stochastic forcing, which has a Gaussian distribution with zero mean and variance:

$$\langle f_i(t, \vec{x}) f_j(t', \vec{x}') \rangle = \delta(t - t') N_{L^{-1}, ij}(|\vec{x} - \vec{x}'|), \quad (3)$$

where $\langle \cdot \rangle$ denotes the ensemble average over the realizations of f . This correlator is local in time, to preserve Galilean invariance, and is concentrated, in Fourier space, on the inverse of the integral scale L [48]. The stochastically forced NS equation (2) can then be represented as a field theory following the standard Martin–Siggia–Rose–Janssen–de Dominicis response functional formalism [49–51], which by essence includes all the fluctuations. In the RG treatment, the integration of these fluctuations is achieved *progressively* in the wave-number space, and yields a *renormalization flow*. Any n -point correlation function $G^{(n)}$ between velocity or pressure fields can be simply expressed in the field theory from the cumulant generating functional and obeys an exact RG flow equation.

However, the flow equation for $G^{(n)}$ involves $G^{(n+1)}$ and $G^{(n+2)}$ which results in an infinite hierarchy of flow equations that needs to be solved.

It was realized in [31,47] that these flow equations can be closed exactly in the limit of large wave numbers using the symmetries of the NS field theory (or more precisely extended symmetries). Indeed, symmetries play a key role in field theory in general, since they yield exact relations between correlation functions known as *Ward identities*. It turns out that the NS field theory possesses two extended symmetries, the time-dependent Galilean symmetry and a time-dependent shift symmetry recently unveiled [52], which can be exploited to achieve the exact closure of the hierarchy of flow equations at large wave numbers. Moreover, these flow equations can be solved analytically at the fixed point, which corresponds to the stationary turbulent state. Let us now give the result for the (transverse part of the) velocity-velocity correlation function C defined as

$$C(t, \vec{k}) \equiv \text{TF}(\vec{v}(t_0 + t, \vec{x}_0 + \vec{x}) \cdot \vec{v}(t_0, \vec{x}_0)), \quad (4)$$

TF denoting the Fourier transform with respect to \vec{x} . At small time lag t , $C(t, \vec{k})$ takes the form

$$C(t, \vec{k}) = A\epsilon^{2/3}k^{-11/3} \exp[-\gamma(\epsilon L)^{2/3}(tk)^2 + O(k)], \quad (5)$$

where γ and A are nonuniversal constants [31], ϵ is the mean energy dissipation rate, and L is the integral scale. The leading term in k^2 in the exponential is exact, whereas the factor in front of the exponential is not. Indeed, the exponent of the power law could be modified by terms of order $\ln(k)$ in the exponential, entering in the indicated $O(k)$ corrections. The leading behavior of the correlation function at large wave numbers is hence a Gaussian in the variable tk , which is not the expected scaling variable. Indeed, dimensional analysis (Kolmogorov theory) predicts a dynamical critical exponent $z = 2/3$ and thus a scaling variable $tk^z = tk^{2/3}$. The dependence in tk is thus a breaking of standard scale invariance, generated by intermittency, and induces an explicit dependence in the integral scale L . An effective value $z = 1$ for the dynamical exponent is a large correction. This effect is often described phenomenologically as the random sweeping effect [5,53].

The energy spectrum can be described in the dissipative range by taking the appropriate $t \rightarrow 0$ limit [33]. One can assume that the scaling variable $tk^{2/3}$ saturates when t approaches the Kolmogorov timescale $\tau_K = \sqrt{\nu/\epsilon}$ and k reaches L^{-1} , since these are the two relevant scales, such that $tk^{2/3} \rightarrow \tau_K L^{-2/3}$. One thus obtains for the energy spectrum $E(k) \equiv \lim_{t \rightarrow 0} 4\pi k^2 C(t, k)$ the expression

$$E(k) = A' \epsilon^{2/3} (k\eta)^{-\beta} \exp[-\mu(k\eta)^\alpha], \quad (6)$$

where $\beta = 5/3$, $\alpha = 2/3$, and μ and A' are positive nonuniversal constants related to γ and A , respectively. This behavior is valid at large wave numbers that are still controlled by the fixed point, which should correspond to the NDR. Indeed, in the FDR, for very small spatial scales, the spectrum should be regularized by the viscosity and should be analytical in real space, which means that it should decay as a pure exponential in k space. The unusual emergence of a stretched exponential behavior is the manifestation of the violation of standard scale invariance. In standard scale invariance, there would be no transitional regime between the inertial regime and the FDR. The value $\alpha = 2/3$ arises from the discrepancy between the Kolmogorov dynamical exponent and the effective one. Note that the emergence of this stretched exponential was also related in [30] to intermittency, and more precisely to intermittent energy transfers. It is indeed shown that the stretched exponential is removed by filtering out in time series of the energy spectrum the large intermittent bursts in energy at high wave numbers.

The main purpose of this paper is to attest the value of the exponent α in the exponential, and thereby to test the assumption of saturation of the scaling variable. Since the NPRG theory does not determine the prefactor of the exponential [as explained in our comment of (5)], we use a method which allows us to estimate α irrespective of the precise form of this prefactor, as follows. Extracting

the value of α from the expression of the first logarithmic derivative of (6),

$$D_1(k\eta) = \frac{d \ln(E)}{d \ln(k\eta)} = -\beta - \mu\alpha(k\eta)^\alpha, \quad (7)$$

would require a three-parameter nonlinear fit, which is not realistic given the typical extent of the NDR and quality of the data in this range. Previous works evidenced the high sensibility of such fits to the range of fitting or the initial condition of the fit algorithm [30]. Our analysis concentrates on the second and third logarithmic derivatives defined as

$$D_2(k\eta) = \frac{d(-D_1)}{d \ln(k\eta)} = \mu\alpha^2(k\eta)^\alpha, \quad (8)$$

$$D_3(k\eta) = \frac{d \ln(D_2)}{d \ln(k\eta)} = \alpha. \quad (9)$$

In a log-log scale, the curve of D_2 in the dissipative range is expected to be a line with slope α , while the curve of D_3 is expected to exhibit a plateau in this range of height α . Beyond reducing the number of fit parameters, the main advantage of D_2 and D_3 is to provide a method to eliminate the contributions from subleading terms in the exponential of Eq. (5). Let us note that previous works predicted the existence of an energy pileup, called the bottleneck effect, leading to a bump of the compensated spectrum in the transitional regime between the IR and the NDR [15,55]. At the theoretical level, this effect modifies the prefactor of the exponential, which we do not try to resolve here. The numerical and experimental spectra we have analyzed do not show any noticeable bottleneck effect. However, it plays no role in the following analysis since it is eliminated in the higher derivatives D_2 and D_3 studied here. In the following, we first analyze the spectra obtained from DNS in the dissipative range, and then present the analysis of the experimental data.

III. NUMERICAL DATA

A. Numerical simulations

We obtain the numerical energy spectra from DNS of the NS equation under fully random large-scale forcing and in isotropic and homogeneous conditions. The turbulent flow is simulated in a cubic periodic domain of size 2π with the same resolution in each of the coordinate directions. The Navier-Stokes equation is solved with the use of a pseudospectral parallelized code; time advancement is implemented with the second-order Runge-Kutta scheme [54]. The simulation parameters are determined by the Taylor microscale Reynolds number (Re_λ) and the value of $k_{\max}\eta$, where k_{\max} is the maximal wave number resolved in the spectrum. We perform a sequence of simulations with fixed Re_λ and increasing grid resolution. In the first run the computational grid size is chosen to ensure at least $k_{\max}\eta = 1.5$ which is commonly accepted as an adequate spatial resolution for DNS. In the following runs the solution obtained in previous steps is transferred to a finer computational grid with resolution $N \rightarrow 2N$, while the Re_λ and the forcing scales are unchanged. By doing so, we increase twofold the value of $k_{\max}\eta$ and we therefore get access to smaller scales in the dissipative range of the turbulence spectrum. The values of the Taylor Reynolds number, size of the computational grid, and associated value of $k_{\max}\eta$ used in the simulations are summarized in Table I.

The spectra obtained for each Re_λ and resolution, averaged over space and time once the stationary state is reached, are displayed in Fig. 1. They exhibit an inertial range extending from about half a decade at $\text{Re}_\lambda = 60$ to about a decade and a half at $\text{Re}_\lambda = 240$. In this range, the spectra decay as power laws with an exponent K depending on the Re_λ . These values are represented in Fig. 4, together with the experimental results. Both results are in agreement. Clearly, the determination of the exponent K from the DNS spectra is not very precise, as the Re_λ is limited, compared to standard DNS with $k_{\max}\eta \simeq 1.5$. Let us recall that in this paper we have chosen to favor the resolution over the extent of the inertial range, in order to increase the accuracy on the

TABLE I. Parameters of the simulations: Maximal wave number $k_{\max}\eta$ as a function of the Taylor microscale Reynolds number Re_λ and the grid resolution N .

| $N \setminus Re_\lambda$ | 60 | 90 | 160 | 240 |
|--------------------------|------|------|-----|-----|
| 256 | 3.0 | 1.5 | | |
| 512 | 6.0 | 3.0 | 1.5 | |
| 1024 | 12.0 | 6.0 | 3.0 | 1.5 |
| 2048 | | 12.0 | 6.0 | 3.0 |

determination of α . However, compared to previous works focused on the dissipation range, we choose a somewhat lower resolution (but still sufficient to resolve the NDR) while reaching a higher Re_λ [30].

The first logarithmic derivatives D_1 , defined by (7), of the DNS spectra are shown in Fig. 2. Their behaviors are very similar to the ones obtained in previous works [23,24,30]. In particular, one distinguishes two qualitatively different regimes: the NDR up to $k\eta \approx 4$, and the FDR extending beyond this value. In the NDR, the D_1 curves exhibit a slight convex curvature, more visible as the Re_λ increases, which indicates that $\alpha < 1$ in this region. In the FDR, the curves of D_1 appear reasonably linear in log-log scale, indicating a pure exponential decay $\alpha \simeq 1$. Moreover, the curves do not collapse in this range, suggesting that this regime is not universal. These observations are in good agreement with previous studies, and lead in particular to the two-exponential model of [30], one with $\alpha < 1$ dominant in the NDR, and the other one with $\alpha = 1$ in the FDR.

B. Analysis of the numerical spectra in the near-dissipative range

In order to push further the previous observations, and to obtain a precise determination of the exponent α in the NDR, we compute the second and third logarithmic derivatives defined by (8) and (9) for the DNS spectra of Fig. 1. Our numerical data are smooth enough to allow for the numerical evaluation of the successive derivatives by finite differences.

The result for the third derivative is displayed in Fig. 3, for the different Re_λ 's. The results for the second derivative show very similar features. The D_3 curves clearly exhibit a plateau for values of $k\eta$ in the NDR, in agreement with the theoretical expression (9). The value of this plateau is smaller than 1, and appears to be very close to the NPRG prediction $\alpha = 2/3$. The inset is a magnification of the plateau, which shows that α is close to 1 at small Re_λ and approaches the value $\alpha = 2/3$ as

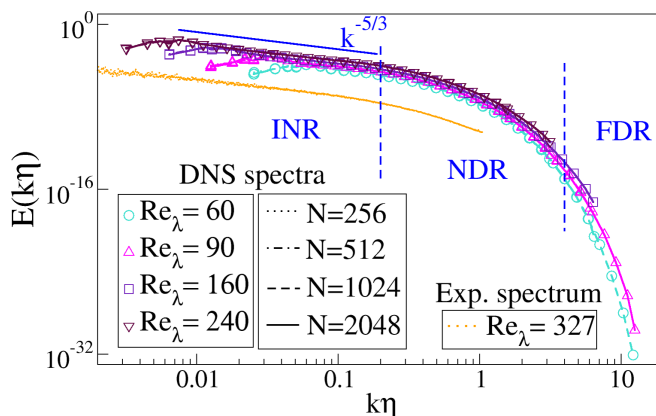


FIG. 1. Spectra obtained from DNS, for the set of Re_λ and resolutions N given in Table I. In all the figures, INR, NDR, and FDR stand for inertial range, near-dissipative range, and far-dissipative range, respectively.

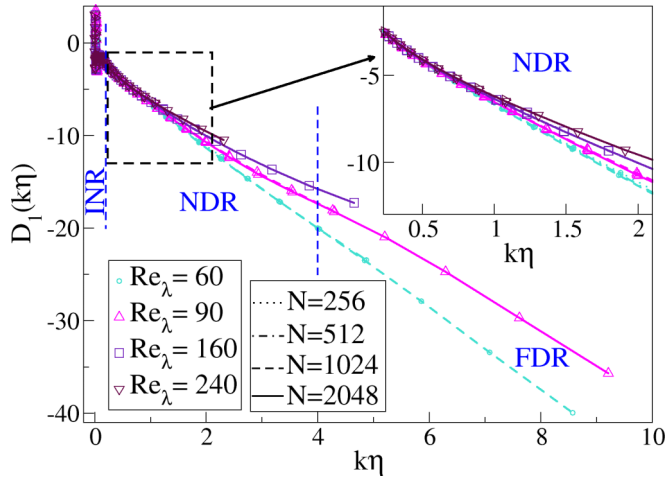


FIG. 2. First logarithmic derivative D_1 of the spectra of Fig. 1, with the inset showing a zoom in the near-dissipative range. These results are very similar to those obtained in previous works [23,24,30]. In particular, D_1 is not linear in the NDR, hence it is not compatible in this range with a pure exponential behavior ($\alpha = 1$).

the Re_λ grows. This is in excellent agreement with [30], where they find a value of α in the NDR decreasing as Re_λ increases, down to $\alpha \simeq 0.78$ for their highest $Re_\lambda = 89$ (we find $\alpha \simeq 0.77$ for $Re_\lambda = 90$; see Fig. 5).

The average value of α on the plateau is represented in Fig. 5 as a function of the Re_λ , together with the experimental results. Both results are in agreement. The extent of the NDR seems to remain $0.2 \lesssim k\eta \lesssim 4$ independently of the Re_λ . Interestingly, one observes that, for the spectra at lower Re_λ , D_3 departs from the plateau at higher wave numbers—in the FDR, towards a value which we anticipated as 1, which would signal the setting of the regular (simple exponential) behavior. However, the expected value $\alpha = 1$ cannot be quite reached in the DNS because of the truncation of wave numbers at a finite k_{\max} .

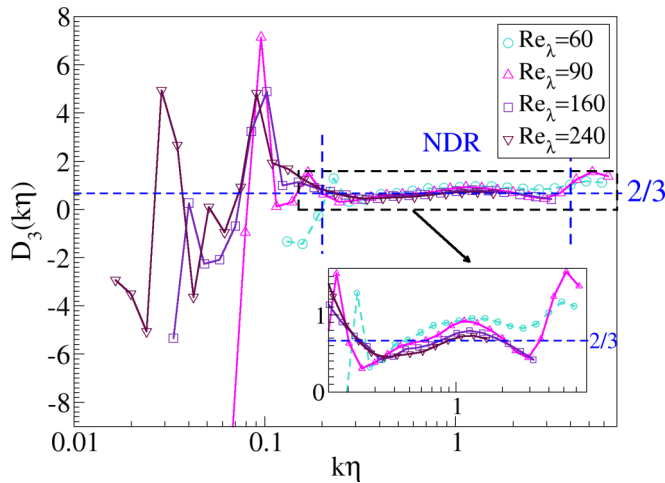


FIG. 3. Third logarithmic derivative, defined by (9), computed for the DNS spectra of Fig. 1, with the inset showing a zoom in the near-dissipative range. Only the curves for the highest resolution for each Re_λ are shown for clarity. They all show a plateau in the NDR, the value of which is α , which approaches $2/3$ as the Re_λ increases.

The analysis of the numerical spectra is thus in quantitative agreement with the theoretical prediction $\alpha = 2/3$, and provides useful indications to guide the analysis of the experimental data.

IV. EXPERIMENTAL DATA

A. Data preprocessing

Let us describe the experimental data of grid turbulence acquired in the S1MA wind tunnel at Modane (ESWIRP project). The data are made of velocity time series recorded by four hot wires at a frequency of 250 kHz, with durations ranging from 3 to 10 min each. The turbulent flow source blows air at speed ranging from 20 to 45 m s⁻¹, resulting in a variety of values for Re_λ . The distance of the hot wires from the grid ranges from 7.9 to 23.16 m [35]. We analyze all the recordings using a systematic procedure described below, focusing on the energy spectra.

We divide the recordings into samples of equal time duration $\Delta t = 20$ s (respectively $\Delta t = 60$ s). This provides us with a total number of 3840 (respectively, 1176) samples, which we analyze separately. We use the Taylor hypothesis to express the velocity as a function of the longitudinal space coordinate. For each sample, we compute the third-order structure function $S_3(\ell) = \langle (\delta u_\ell)^3 \rangle$ where δu_ℓ is the longitudinal velocity increment $\delta u_\ell = [\vec{u}(\vec{r} + \vec{\ell}) - \vec{u}(\vec{r})] \cdot \vec{\ell}/|\vec{\ell}|$. We determine the corresponding average injection/dissipation rate per unit mass ϵ from the plateau value of S_3 using the four-fifths law: $\epsilon = -\frac{5}{4}S_3(\ell)/\ell$ in the inertial range. We then compute the associated Kolmogorov scale as $\eta = \nu^{3/4}\epsilon^{-1/4}$, with $\nu = 1.5 \times 10^{-5}$ m² s⁻¹ the air kinematic viscosity. The Taylor microscale Reynolds number for each sample is deduced using the isotropic relation $\text{Re}_\lambda = u_{\text{rms}}\sqrt{15/\nu\epsilon}$. Let us note that the determination of ϵ through the four-fifths law is not very precise, and thus it entails some error on the Re_λ . However, we also used another determination of ϵ , through the position of the peak of the dissipative spectrum $k^2E(k)$, and we checked that this does not change the different distributions shown here, nor the final value of α .

We compute the kinetic-energy spectrum of each sample by performing a discrete Fourier transform (the fast Fourier-transform algorithm) and rescale it as a function of the dimensionless wave number $k\eta$. (A typical spectrum is displayed at the top of Fig. 10.) We smoothen the spectra out using a regular binning of 20,000 bins in $\ln(k\eta)$ scale. In the experimental spectra, $k\eta$ typically ranges from 10^{-3} to 3.5. The quality and the extent in wave number of the spectra vary quite substantially between the samples. The variability of the measurement quality comes from the fact that the wind tunnel is an open facility in which dust and pollen can enter and affect the hot wires. Because of this issue, some values of ϵ are questionable, which explains why some values of Re_λ are out of the range 200–600. However, all of them appear to increase as functions of k beyond a wave number k_M , which we interpret as a contamination by the small-scale response of the hot wires. The value of k_M depends on the spectra, but is found to be typically $k_M\eta \simeq 3$. In the following, we restrict the analysis to wave numbers below k_M . Note that we do not observe any noticeable bottleneck effect on the experimental spectra analyzed. As this effect is expected to attenuate when the Re_λ increases [56], it would be difficult to detect here; moreover, as already explained, it alters the prefactor of the exponential and disappears in the higher derivatives considered in the present paper.

B. Selection of spectra

In order to assess the quality of each sample and to remove low-quality spectra, we operate a data-driven selection, based on the value of the inertial range exponent K and on the extent of the dissipative range, the determinations of which are detailed in Secs. IV C and IV D, respectively. We first eliminate for both sample durations $\Delta t = 20$ and 60 s the spectra with an exponent K differing from the K41 value by more than 20%. This procedure typically removes very noisy spectra presenting several unphysical large peaks. After this first filtering, there remain 3486 (respectively, 1080) exploitable spectra for $\Delta t = 20$ s (respectively, $\Delta t = 60$ s). We then proceed to a second selection by retaining only the spectra with a large enough dissipative range of width $\Delta(k\eta) > 0.2$.

This second selection removes spectra which are not well resolved in the dissipative range, probably affected by the noise from the sensor. This finally leaves us with 1641 (respectively, 590) spectra, for $\Delta t = 20$ and 60 s. We further analyze and discuss these selected spectra in the following.

C. Inertial range

In this section, we briefly describe the analysis of the spectra in the inertial range. We determine the exponent K of the power-law decay of the energy spectrum $E(k\eta) \sim (k\eta)^{-K}$ in this range, to be compared with the expected K41 value $K \simeq 5/3$. We do not denote it β as in (6) since we do not assume the two exponents to be equal in the inertial and dissipative ranges. We use two methods to estimate K : a direct fit of the log-log spectrum, which is expected to be a line in the inertial range, and a fit of the first logarithmic derivative D_1 , which is expected to present a plateau of value $-K$ in the corresponding range. Throughout this paper, we only use fitting functions which are affine (either lines or constants). The result of a fitting procedure is in general sensitive to the precise fitting interval chosen, and to the chosen precision criterion. In order to reduce as much as possible these effects, we devise an optimized algorithm, described in the Appendix, the goal of which is to search for the largest interval with the minimal error where an affine behavior is present. For each spectrum, we apply this fitting algorithm to both the log-log spectrum and the corresponding D_1 , and compare these two results. If the relative difference in the obtained K is less than 2%, we take the average value. Otherwise we keep the estimate for K which corresponds to the largest interval.

We present in Fig. 4 the results for the exponent K as a function of the Re_λ , for the two sample durations $\Delta t = 20$ and 60 s. The experimental data correspond to Re_λ distributed between 25 and 1150, among which more than 90% lie between 150 and 650. Their distribution is represented in the inset of Fig. 4, using bins of width $\Delta \text{Re}_\lambda = 25$, and computing within each bin the average and the standard deviation of the decay exponent K . The error bars in Fig. 4 represent the standard deviation within each bin, irrespective of the total number of spectra they contain. Note that the weight of the different points is thus very different: for instance, the first points at low Re_λ represent very few spectra. We observe that the value of the inertial exponent K grows with the Re_λ , to reach a value close to $K = 5/3$ for $\text{Re}_\lambda \gtrsim 600$. The results for both durations are in close agreement. However, let us emphasize that this determination is not accurate enough to detect the corrections due to intermittency, which are expected to increase by about 5% the K41 value $K = 5/3$. The error bars of the points around $\text{Re}_\lambda = 600$ obtained for the duration 20 s are typically representative since they correspond to a large number of spectra, and they clearly exceed the 5% level of tolerance needed to estimate intermittency corrections on the inertial range exponent.

D. Near-dissipative range and stretch exponent

In this section, we turn to the analysis of the near-dissipative range. As for the DNS data, we rely for the experimental data on two independent estimations of the stretch exponent α : one from the second logarithmic derivative D_2 given by (8) and one from the third one D_3 given by (9). The experimental data are much less smooth than the numerical ones, such that performing simple finite differences to compute numerical derivatives generates a lot of noise, which would spoil the accuracy of this procedure. For this reason, we resort to a more reliable computation of the derivatives, described in the Appendix. We obtain two determinations of α denoted α_2 and α_3 , from the optimized linear fitting of D_2 in log-log scale and from applying to D_3 the same optimized algorithm to search for a plateau, respectively. We only retain estimations of α for which the error of the associated fit is less than $Q = 10^{-1}$ (see the Appendix for the definition of Q).

We present in Fig. 5 the results obtained for α_2 and α_3 as functions of the Re_λ , for both sample durations $\Delta t = 20$ and 60 s. The distribution of Re_λ corresponding to the four sets of spectra are displayed in Fig. 6. The large majority of spectra presents a Re_λ again lying in the range $200 \lesssim \text{Re}_\lambda \lesssim 500$. The number of spectra with a Re_λ outside this range is negligible. Contrary to the inertial exponent K , we do not observe for α a clear dependence on the Re_λ (at least not within

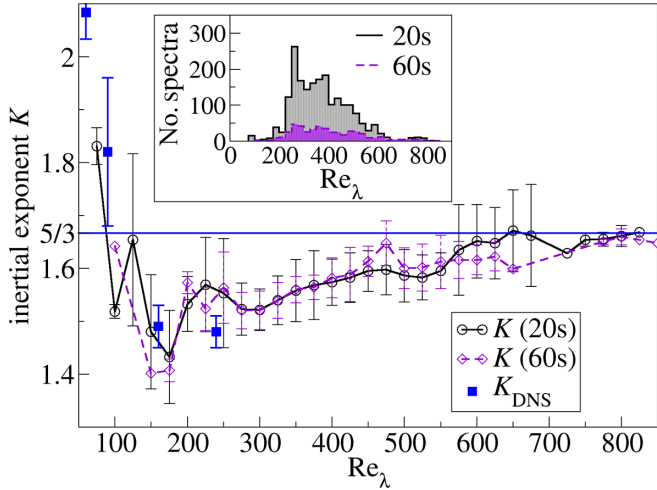


FIG. 4. Exponent K of the power law in the inertial range, from DNS and from experiments for both sample durations $\Delta t = 20$ and 60 s, as a function of the Taylor microscale Reynolds number. For the experimental points, the symbols represent the mean values of K on each Re_λ bin, and the error bars represent the standard deviation within each bin. The numbers of spectra in each bin are not equal; they are given by the distribution shown in the inset.

the present level of accuracy), but rather a constant value (up to fluctuations) smaller than 1. The error bars in Fig. 5 represent the standard deviation within each Re_λ bin, and do not reflect the fact that some bins (at lower or larger Re_λ) contain very few spectra. Moreover, one notices that the estimation of α_2 appears systematically larger than the one from α_3 . The determination of α_2

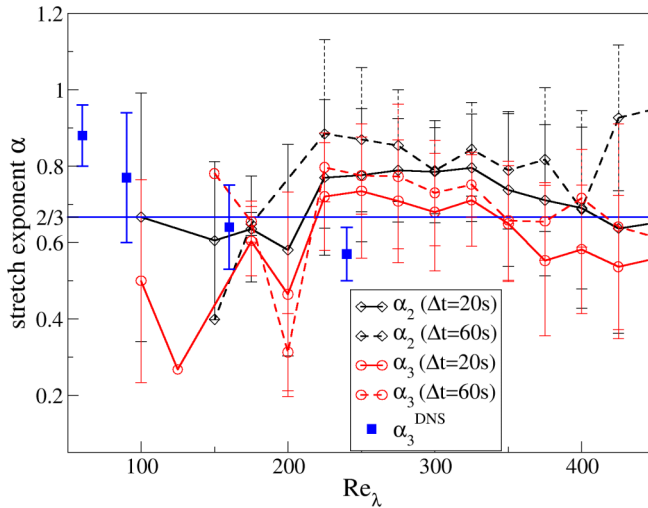


FIG. 5. Stretch exponent α as a function of the Taylor microscale Reynolds number from DNS and from experiments: α_2 (black lines with diamonds) computed from D_2 and α_3 (red lines with triangles) computed from D_3 , for experimental spectra corresponding to both durations $\Delta t = 20$ (plain lines) and 60 s (dashed lines), and α_3 (blue squares) from DNS. For the experimental points, the symbols indicate the mean values of α for each Re_λ bin, and the error bars represent the standard deviation within each bin. The numbers of spectra in each bin are not equal; the distribution of Re_λ for each set of spectra is represented in Fig. 6.

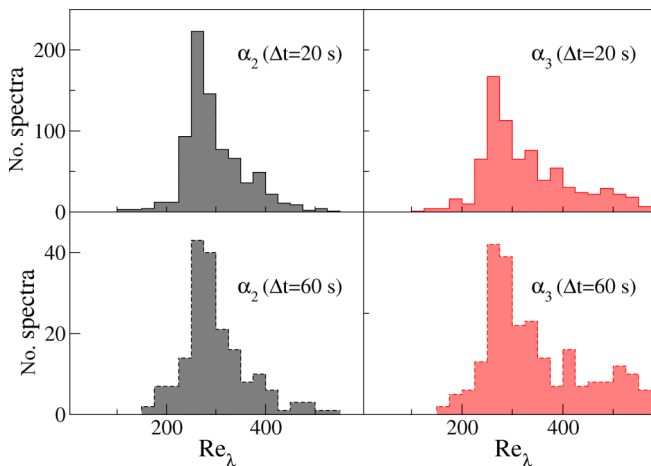


FIG. 6. Distribution of the Re_λ corresponding to each set of data displayed in Fig. 5, for the two sample durations $\Delta t = 20$ and 60 s, and for the two methods D_2 and D_3 .

involves a two-parameter fit, such that the resulting value for α_2 is expected to be less precise than the one of α_3 , but we have no interpretation for the seemingly systematic overestimation.

Since we did not find any sizable dependence of the stretch exponent α on the Re_λ , we rather concentrate in the following on the distributions of the values of α . We present in Fig. 7 these distributions for the same data as those used in Fig. 5, that is, both α_2 and α_3 and for both sample durations. One notices again that the distributions for α_2 are slightly shifted upward with respect to the ones for α_3 . The averages and standard deviations of all the distributions are gathered in Table II. The distributions presented in Fig. 7 correspond to an error tolerance of $Q = 10^{-2}$. We studied the influence of this precision criterion by varying it from 10^{-1} to 10^{-4} . The corresponding distributions for α_3 are displayed in Fig. 8. It is remarkable that the more stringent the precision criterion the narrower the distributions around the theoretical prediction $\alpha = 2/3$. In fact, very few spectra pass the highest-precision criterion $Q = 10^{-4}$ for the sample duration $\Delta t = 60$ s, and none pass for $\Delta t = 20$ s.

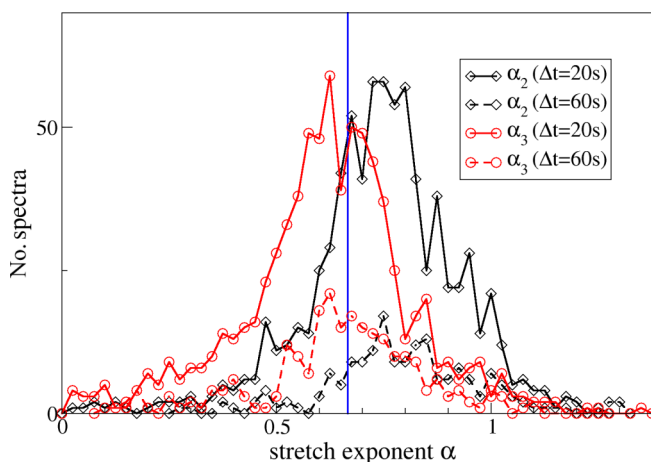


FIG. 7. Distribution of the stretch exponent α : α_2 (black lines with diamonds) computed from D_2 and α_3 (red lines with triangles) computed from D_3 , for spectra corresponding to both durations $\Delta t = 20$ (plain lines) and 60 s (dashed lines). The mean value and standard deviation of these distributions are reported in Table II.

TABLE II. Summary of the number of spectra (no.), average value ($\langle\alpha\rangle$), and standard deviation (σ) of the distributions of the stretch exponent α obtained from either the second (α_2) or the third (α_3) logarithmic derivatives, for spectra of both sample durations $\Delta t = 20$ and 60 s, and for different precision tolerances Q on the fit.

| α_i | Δt | Q | No. | $\langle\alpha\rangle$ | σ |
|------------|------------|-----------|------|------------------------|----------|
| α_2 | 20 s | 10^{-1} | 792 | 0.754 | 0.181 |
| | | 10^{-2} | 785 | 0.757 | 0.176 |
| | | 10^{-3} | 685 | 0.782 | 0.151 |
| | | 10^{-4} | 282 | 0.756 | 0.126 |
| | 60 s | 10^{-1} | 178 | 0.805 | 0.188 |
| | | 10^{-2} | 175 | 0.812 | 0.178 |
| | | 10^{-3} | 162 | 0.833 | 0.159 |
| | | 10^{-4} | 99 | 0.829 | 0.126 |
| α_3 | 20 s | 10^{-1} | 2892 | 0.621 | 0.226 |
| | | 10^{-2} | 1798 | 0.661 | 0.194 |
| | | 10^{-3} | 89 | 0.678 | 0.167 |
| | | 10^{-4} | 0 | | |
| | 60 s | 10^{-1} | 878 | 0.690 | 0.224 |
| | | 10^{-2} | 703 | 0.719 | 0.190 |
| | | 10^{-3} | 153 | 0.730 | 0.151 |
| | | 10^{-4} | 4 | 0.710 | 0.052 |

To give a final number for α , we can favor the most precise determination, which is α_3 . We retain the two precision criteria $Q = 10^{-2}$ and 10^{-3} , which embody a reasonable compromise between the level of accuracy and the level of statistics. Finally, since the spectra for both sample durations constitute independent sets of comparable qualities, we can consider a weighted average of these results, which yields

$$\langle\alpha_3\rangle_{10^{-2}} \simeq 0.677 \pm 0.193, \quad \langle\alpha_3\rangle_{10^{-3}} \simeq 0.712 \pm 0.157.$$

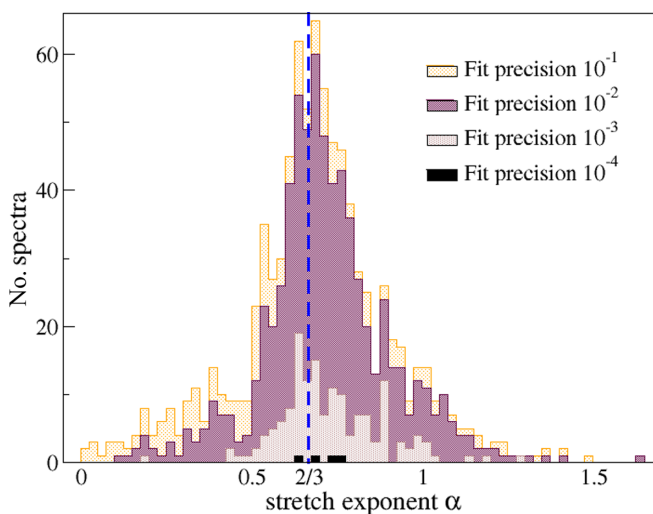


FIG. 8. Distribution of the stretch exponent α_3 for $\Delta = 60$ s and for different precision criteria Q from 10^{-1} to 10^{-4} .

TABLE III. Average value and standard deviation of the distributions of the parameters μ and β obtained for spectra of both sample durations $\Delta t = 20$ and 60 s, and for different precision tolerances Q on the fit.

| Δt | Q | No. | $\langle \mu \rangle$ | σ_μ | $\langle \beta \rangle$ | σ_β |
|------------|-----------|-----|-----------------------|--------------|-------------------------|----------------|
| 20 s | 10^{-1} | 750 | 4.51 | 1.26 | 0.92 | 0.26 |
| | 10^{-2} | 747 | 4.51 | 1.26 | 0.92 | 0.26 |
| | 10^{-3} | 672 | 4.46 | 1.23 | 0.93 | 0.27 |
| | 10^{-4} | 275 | 4.53 | 1.07 | 0.87 | 0.25 |
| 60 s | 10^{-1} | 173 | 4.16 | 1.54 | 0.99 | 0.27 |
| | 10^{-2} | 172 | 4.19 | 1.51 | 0.98 | 0.26 |
| | 10^{-3} | 162 | 4.06 | 1.28 | 1.00 | 0.23 |
| | 10^{-4} | 99 | 3.90 | 0.89 | 1.00 | 0.19 |

Both estimates are very close, since their one- σ intervals are, respectively, $\alpha \in [0.48 : 0.87]$ and $[0.55 : 0.87]$. We hence choose as a representative final result

$$\langle \alpha \rangle \simeq 0.68 \pm 0.19.$$

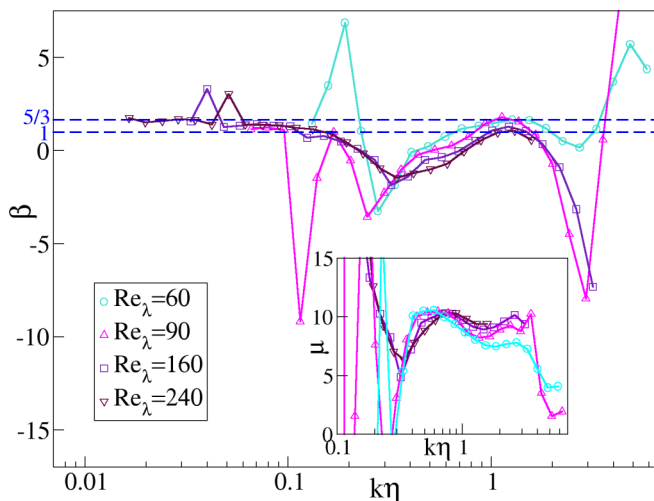
The present analysis indicates that values $\alpha < 0.4$ or $\alpha > 0.9$ can be reasonably excluded.

E. Near-dissipative range: Other parameters

For completeness, we also give in this section the results for the other parameters of (6): the multiplicative constant μ in the exponential, and the exponent β of the power law. The parameter μ can be obtained from the constant $\mu\alpha^2$ in the linear fit of D_2 in log-log scale according to (8). The values found for the experimental data are given in Table III. If we consider, as we do for α , the weighted average of both sample durations for $Q = 10^{-2}$, we obtain

$$\langle \mu \rangle \simeq 4.45 \pm 1.31,$$

which turns out to be of the same order as values found in previous studies [34], although μ is not expected to be universal. In the numerical data, we obtain somewhat higher values, of order 10, as shown in Fig. 9.


 FIG. 9. Parameters β (main graph) and μ (inset) obtained for the DNS spectra of Fig. 1.

The value of β can be computed as

$$\beta = \frac{D_2(k\eta)}{D_3(k\eta)} - D_1(k\eta). \quad (10)$$

However, the precision on β is very poor, and it is highly sensitive to the value found for α . As an indication, we find in the experimental data values close to 1, as summarized in Table III. For instance, for $Q = 10^{-2}$, we obtain from the weighted average of both sample durations

$$\langle\beta\rangle \simeq 0.93 \pm 0.26.$$

In the DNS, the value obtained for β is shown in Fig. 9. It turns out to be close to $\beta = 5/3$, i.e., to the inertial range value, at small Re_λ , and to tend to a smaller value very close to $\beta = 1$ as Re_λ increases, in agreement with the results from the experimental data. But once again, these estimates should be taken with caution. Given the typically small extent of the NDR, the determination of the leading behavior, through α , is already challenging, such that a precise determination of the subleading one, through β , is beyond the reach of the present paper.

V. CONCLUSION

In this paper, we analyze the near-dissipative range of kinetic-energy spectra obtained from high-resolution DNS and from experimental grid turbulence in the Modane wind tunnel in order to test the NPRG prediction of a stretched exponential behavior $E \propto \exp[-\mu(k\eta)^\alpha]$ with exponent $\alpha = 2/3$ in this range. We use two independent determinations, from the second and from the third logarithmic derivatives of the spectra, to estimate the value of α . All the results, from DNS and from experiments, and from the different determinations, are consistent, and yield an estimate for the stretch exponent $\alpha \simeq 0.68 \pm 0.19$, in full agreement with the theoretical prediction.

Let us emphasize that the typically small extent of the near-dissipative range and the level of precision currently accessible in DNS or experimental data do not seem sufficient to reliably determine the prefactor of the exponential, that is, the precise form of the power laws. Hence, the present analysis does not allow us to shed a new light on this point. It could possibly be refined in the future if data with still higher resolution become available. Moreover, it would be also very interesting to further test the NPRG predictions concerning the time dependence of two- or multipoint correlation functions, in DNS or in experiments which dispose of suitable measurement techniques.

ACKNOWLEDGMENTS

L.C. and V.R. gratefully thank N. Wschebor for fruitful discussions and useful suggestions. We acknowledge the European Commission for its support and access to the ONERA operated S1MA wind tunnel through the European Strategic Wind tunnels Improved Research Potential (ESWIRP) project (Project No. FP7/2007-2013 under Grant No. 227816). This work received support from the French Agence Nationale de la Recherche (ANR) through the project NeqFluids (Grant No. ANR-18-CE92-0019). The simulations were performed using the high-performance computing resources from Grand Instrument National de Calcul Intensif (GENCI) of the Institut du Développement et des Ressources en Informatique Scientifique (IDRIS) (Grant No. 020611). G.B. and L.C. are grateful for the support of the Institut Universitaire de France (IUF).

APPENDIX: NUMERICAL PROCEDURES

1. Optimized linear fitting algorithm

Extracting the inertial or dissipative exponents from the experimental data always amounts to an affine fit (either lines in log-log representation or constants). For this, we use an elementary linear regression. However, the accuracy of the result of such a fit strongly depends on the choice of the

fitting domain D , which is delicate since there is no clear delimitation of the inertial or dissipative ranges. Let us denote by $a(D)$ and $b(D)$ the real numbers such that the standard linear fit in the domain D is the affine function $x \mapsto f(x) = a(D)x + b(D)$ and by x_i a data point in the domain D , i.e., $x_i \in D$, and $y_i = f(x_i)$.

To determine the best fitting domain, we use an optimized method based on the alignment of data points in a given domain D . The alignment $\lambda(D)$ is the largest absolute deviation of a data point from the linear fit performed in this domain: $\lambda(D) = \max_{x_i \in D} |a(D)x_i + b(D) - y_i|$. Based on $\lambda(D)$, our algorithm seeks the largest domain $D(\varepsilon)$ such that $\lambda(D) < \varepsilon$ for any given positive number ε . ε stands as a quality requirement of the input data. We estimate the quality $Q(D)$ of the result using the standard error $Q = \sigma/\sqrt{n}$ where σ is the standard deviation and n is the number of data points in the domain. Assembling these elements, we determine the value ε_{opt} that minimizes the function $Q[D(\varepsilon)]$ and use $D(\varepsilon_{\text{opt}})$ as the optimal domain. This procedure is used to determine the inertial exponent K of the spectrum and the stretch exponent α from the second logarithmic derivative $D_2(k\eta)$.

We use the same procedure to find the optimal plateau, i.e., the optimal domain where the curve has the lowest slope. This is achieved by replacing Q by $Q'(D) = Q(D) + |a(D)|$, where $a(D)$ is as before the slope of the linear fit in the domain D . We use this method to determine the inertial exponent K from the first logarithmic derivative $D_1(k\eta)$ and for the stretch exponent α_3 from the third logarithmic derivative $D_3(k\eta)$. The value of Q is recorded for each estimate, and is used as a precision indicator for the quality of the fit. In particular, we rely on Q to set up a different precision

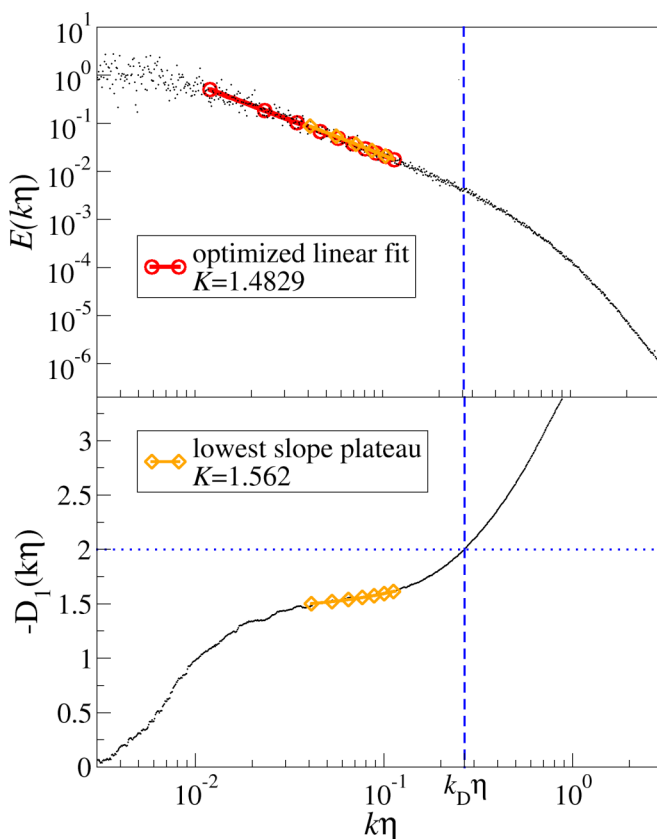


FIG. 10. Result of the optimized fitting algorithm for the determination of K from the log-log spectrum (red line with circles) and from the first logarithmic derivative D_1 (orange line with diamonds). The result from D_1 is reported on the spectrum E for comparison.

criterion, e.g., in Fig. 8 or Table II. The application of these procedures is illustrated in Sec. A 3 on a typical spectrum.

2. Numerical computation of derivatives for the experimental data

As explained in Sec. IV D, the direct computation by finite differences of successive derivatives of the experimental spectra is too noisy to be exploitable. Instead, to smooth out the data, we use the following procedure. The derivative of a function at a certain point is computed by implementing a linear fit in a window D centered around this point containing a fixed number of data points (we typically use windows of 50 points). The linear fit coefficient $a(D)$ is thus an estimate of the value of the derivative at this point. By sliding the window D through all the data points, we obtain the derivative of the whole function. The logarithmic derivatives of the type $d \ln f / d \ln q$ are performed using the same method with a power-law fit [fitting function $q \mapsto b(D)q^{a(D)}$] and the derivatives of the type $d/d \ln q$ with an exponential fit [fitting function $q \mapsto b(D)e^{a(D)q}$]. With this procedure, the resulting derivatives of the experimental spectra are smooth enough to serve for further analysis.

3. Illustration of the determination of the exponents K and α

As an illustration of the procedures described above, we present their result on a typical spectrum. The determination of K is illustrated in Fig. 10, which shows this particular spectrum $E(k\eta)$ in

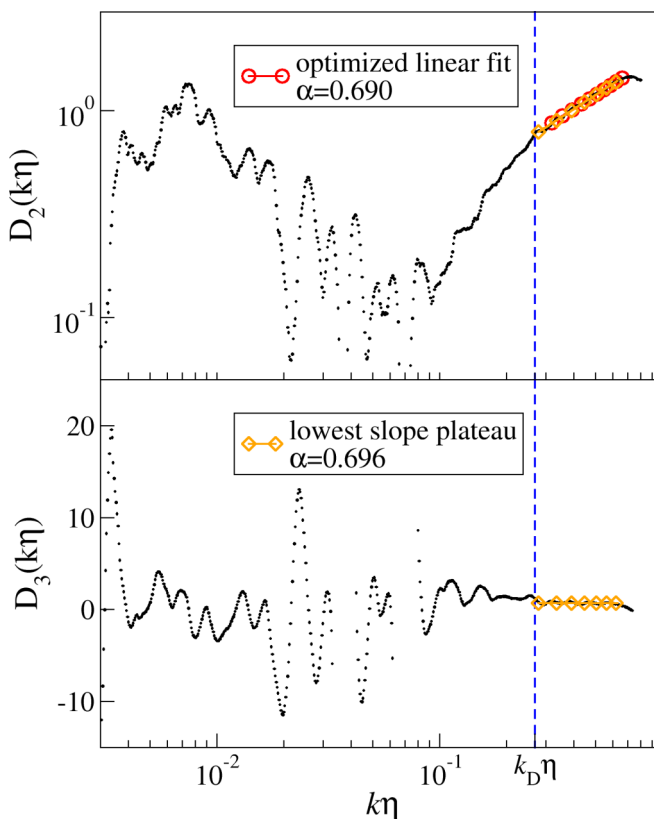


FIG. 11. Result of the optimized fitting algorithm for the determination of α from the second (red line with circles) and from the third (orange line with diamonds) logarithmic derivatives of the spectrum. The result from D_3 is reported on the D_2 curve for comparison.

log-log scale and its first logarithmic derivative $D_1(k\eta)$, obtained as explained in the previous section. The D_1 curve is first used to estimate the dissipative wave number k_D , which we define as the wave number for which $(k\eta)^2 E(k\eta)$ is maximum, and which hence corresponds to the value $D_1(k_D\eta) = 2$. We find $k_D\eta \simeq 0.18$, which is in agreement with typical values in the literature and also with the value found for the numerical spectra. This value can be used as a reliable upper bound for the inertial range. The search for the largest best domain with linear behavior for E and lowest slope plateau for D_1 is initialized in the range $k\eta \in [0.01, k_D\eta]$. The result of the optimized algorithm is represented, with their respective domains, as the red line with circles and orange line with diamonds, respectively. In this example, the two values for K differ by more than 2% so the value from the linear fit of E is retained since it corresponds to the largest domain.

The determination of α is illustrated in Fig. 11, which shows the second D_2 and third D_3 logarithmic derivatives defined in (8) and (9), respectively. The numerical derivatives are evaluated as described in the previous section. The search domain for the near-dissipative range is initialized as $k\eta \in [k_D\eta, k_M\eta = 3]$. The result of the optimized linear fitting algorithm applied to D_2 to extract α_2 (and $\mu\alpha_2^2$ as the second parameter of the fit) is represented by the red line with circles; the result of the lowest slope plateau algorithm applied to D_3 to extract α_3 is represented by the orange line with diamonds. In this example, the two results are in close agreement.

-
- [1] A. N. Kolmogorov, The local structure of turbulence in incompressible viscous fluid for very large Reynolds numbers, *Dokl. Akad. Nauk SSSR* **30**, 301 (1941)
 - [2] A. N. Kolmogorov, The local structure of turbulence in incompressible viscous fluid for very large Reynolds numbers, *Proc. R. Soc. A* **434**, 9 (1991).
 - [3] A. N. Kolmogorov, Dissipation of energy in locally isotropic turbulence, *Dokl. Akad. Nauk SSSR* **32**, 16 (1941)
 - [4] A. N. Kolmogorov, Dissipation of energy in locally isotropic turbulence, *Proc. R. Soc. A* **434**, 15 (1991).
 - [5] R. H. Kraichnan, The structure of isotropic turbulence at very high Reynolds numbers, *J. Fluid Mech.* **5**, 497 (1959).
 - [6] V. I. Tatarskii, Line of sight propagation fluctuations, in *Atmospheric Turbulence and Radio Wave Propagation*, edited by A. M. Yaglom and V. I. Tatarskii (Nauka, Moscow, 1967), pp. 314–329.
 - [7] M. S. Uberoi and P. Freymuth, Spectra of turbulence in wakes behind circular cylinders, *Phys. Fluids* **12**, 1359 (1969).
 - [8] Y. Pao, Structure of turbulent velocity and scalar fields at large wavenumbers, *Phys. Fluids* **8**, 1063 (1965).
 - [9] A. A. Townsend, On the fine-scale structure of turbulence, *Proc. R. Soc. A* **208**, 534 (1951).
 - [10] E. A. Novikov, Energy spectrum of a turbulent flow of incompressible fluid, *Dokl. Akad. Nauk SSSR* **139**, 331 (1961).
 - [11] A. S. Gurvich, B. M. Koprov, L. R. Tsvang, and A. M. Yaglom, Data on the small-scale structure of atmospheric turbulence, in *Atmospheric Turbulence and Radio Wave Propagation*, edited by A. M. Yaglom and V. I. Tatarskii (Nauka, Moscow, 1967), pp. 30–52.
 - [12] A. S. Monin and A. M. Yaglom, *Statistical Fluid Mechanics: Mechanics of Turbulence*, 2nd ed. (MIT, Cambridge, MA, 1973).
 - [13] C. Foias, O. Manley, and L. Sirovich, Empirical and Stokes eigenfunctions and the far-dissipative turbulent spectrum, *Phys. Fluids A* **2**, 464 (1990).
 - [14] L. Sirovich, L. Smith, and V. Yakhot, Energy Spectrum of Homogeneous and Isotropic Turbulence in Far Dissipation Range, *Phys. Rev. Lett.* **72**, 344 (1994); **74**, 1492 (1995).
 - [15] D. Lohse and A. Müller-Groeling, Bottleneck Effects in Turbulence: Scaling Phenomena in r versus p Space, *Phys. Rev. Lett.* **74**, 1747 (1995).
 - [16] U. Frisch and M. Vergassola, A prediction of the multifractal model: The intermediate dissipation range, *Europhys. Lett.* **14**, 439 (1991).
 - [17] K. R. Sreenivasan, On the fine-scale intermittency of turbulence, *J. Fluid Mech.* **151**, 81 (1985).

- [18] L. M. Smith and W. C. Reynolds, The dissipation-range spectrum and the velocity-derivative skewness in turbulent flows, *Phys. Fluids A* **3**, 992 (1991).
- [19] Z. She and E. Jackson, On the universal form of energy spectra in fully developed turbulence, *Phys. Fluids A* **5**, 1526 (1993).
- [20] S. G. Saddoughi and S. V. Veeravalli, Local isotropy in turbulent boundary layers at high Reynolds number, *J. Fluid Mech.* **268**, 333 (1994).
- [21] T. Sanada and V. Shanmugasundaram, Random sweeping effect in isotropic numerical turbulence, *Phys. Fluids A* **4**, 1245 (1992).
- [22] S. Chen, G. Doolen, J. R. Herring, R. H. Kraichnan, S. A. Orszag, and Z. S. She, Far-Dissipation Range of Turbulence, *Phys. Rev. Lett.* **70**, 3051 (1993).
- [23] D. O. Martinez, S. Chen, G. D. Doolen, and R. H. Kraichnan, Energy spectrum in the dissipation range of fluid turbulence, *J. Plasma Phys.* **57**, 195 (1997).
- [24] T. Ishihara, Y. Kaneda, M. Yokokawa, K. Itakura, and A. Uno, Energy spectrum in the near dissipation range of high resolution direct numerical simulation of turbulence, *J. Phys. Soc. Jpn.* **74**, 1464 (2005).
- [25] J. Schumacher, Sub-Kolmogorov-scale fluctuations in fluid turbulence, *Europhys. Lett.* **80**, 54001 (2007).
- [26] T. Ishihara, T. Gotoh, and Y. Kaneda, Study of high-Reynolds number isotropic turbulence by direct numerical simulation, *Annu. Rev. Fluid Mech.* **41**, 165 (2009).
- [27] M. K. Verma, A. Kumar, P. Kumar, S. Barman, A. G. Chatterjee, R. Samtaney, and R. A. Stepanov, Energy spectra and fluxes in dissipation range of turbulent and laminar flows, *Fluid Dynamics* **53**, 862 (2018).
- [28] O. P. Manley, The dissipation range spectrum, *Phys. Fluids A* **4**, 1320 (1992).
- [29] S. B. Pope, *Turbulent Flows* (Cambridge University, Cambridge, England, 2000).
- [30] S. Khurshid, D. A. Donzis, and K. R. Sreenivasan, Energy spectrum in the dissipation range, *Phys. Rev. Fluids* **3**, 082601 (2018).
- [31] M. Tarpin, L. Canet, and N. Wschebor, Breaking of scale invariance in the time dependence of correlation functions in isotropic and homogeneous turbulence, *Phys. Fluids* **30**, 055102 (2018).
- [32] M. Tarpin, L. Canet, C. Pagani, and N. Wschebor, Stationary, isotropic and homogeneous two-dimensional turbulence: A first non-perturbative renormalization group approach, *J. Phys. A* **52**, 085501 (2019).
- [33] L. Canet, V. Rossetto, N. Wschebor, and G. Balarac, Spatiotemporal velocity-velocity correlation function in fully developed turbulence, *Phys. Rev. E* **95**, 023107 (2017).
- [34] P. Debue, D. Kuzzay, E. W. Saw, F. Daviaud, B. Dubrulle, L. Canet, V. Rossetto and N. Wschebor, Experimental test of the crossover between the inertial and the dissipative range in a turbulent swirling flow, *Phys. Rev. Fluids* **3**, 024602 (2018).
- [35] M. Bourgoin, C. Baudet, S. Kharche, N. Mordant, T. Vandenbergh, S. Sumbekova, N. Stelzenmuller, A. Aliseda, M. Gibert, P.-E. Roche, R. Volk, T. Barois, M. Lopez-Caballero, L. Chevillard, J.-F. Pinton, L. Fiabane, J. Delville, C. Fourment, A. Bouha, L. Danaila, E. Bodenschatz, G. Bewley, M. Sinhuber, A. Segalini, R. Örlü, I. Torrano, J. Mantik, D. Guariglia, V. Uruba, V. Skala, J. Puczyłowski, and J. Peinke, Investigation of the small-scale statistics of turbulence in the Modane S1MA wind tunnel, *CEAS Aeronaut. J.* **9**, 269 (2018).
- [36] C. DeDominicis and P. C. Martin, Energy spectra of certain random-stirred fluids, *Phys. Rev. A* **19**, 419 (1979).
- [37] J. D. Fournier and U. Frisch, Remarks on the renormalization group in statistical fluid dynamics, *Phys. Rev. A* **28**, 1000 (1983).
- [38] L. Smith and S. Woodruff, Renormalization-group analysis of turbulence, *Annu. Rev. Fluid Mech.* **30**, 275 (1998).
- [39] L. T. Adzhemyan, N. V. Antonov, and A. N. Vasil'ev, *The Field Theoretic Renormalization Group in Fully Developed Turbulence* (Gordon and Breach, New York, 1999).
- [40] Y. Zhou, Renormalization group theory for fluid and plasma turbulence, *Phys. Rep.* **488**, 1 (2010).
- [41] K. G. Wilson and J. Kogut, The renormalization group and the ϵ -expansion, *Phys. Rep. C* **12**, 75 (1974).

- [42] J. Berges, N. Tetradis, and C. Wetterich, Non-perturbative renormalization flow in quantum field theory and statistical physics, *Phys. Rep.* **363**, 223 (2002).
- [43] P. Kopietz, L. Bartosch, and F. Schütz, *Introduction to the Functional Renormalization Group*, Lecture Notes in Physics (Springer-Verlag, Berlin, 2010).
- [44] B. Delamotte, An introduction to the nonperturbative renormalization group, in *Renormalization Group and Effective Field Theory Approaches to Many-Body Systems*, edited by J. Polonyi and A. Schwenk, Lecture Notes in Physics (Springer-Verlag, Berlin, 2012).
- [45] P. Tomassini, An exact renormalization group analysis of 3D well developed turbulence, *Phys. Lett. B* **411**, 117 (1997).
- [46] C. Mejía-Monasterio and P. Muratore-Ginanneschi, Nonperturbative renormalization group study of the stochastic Navier-Stokes equation, *Phys. Rev. E* **86**, 016315 (2012).
- [47] L. Canet, B. Delamotte, and N. Wschebor, Fully developed isotropic turbulence nonperturbative renormalization group formalism and fixed point, *Phys. Rev. E* **93**, 063101 (2016).
- [48] Let us emphasize that the precise profile chosen for N is not important as it does not influence the universal properties of the flow, as was shown in [45]. It can also be chosen diagonal in component space, without loss of generality because of incompressibility [47]. Moreover, although one may argue that a forcing uncorrelated in time is not realistic physically it was shown that it plays no role for the universal properties. Indeed, introducing finite time correlations in (3) does not alter the universal properties, as long as these correlations are not too long ranged, as was shown in [57] for the Navier-Stokes equation with a power-law forcing and in [58] for the Burgers equation with both short-range and power-law forcing.
- [49] P. C. Martin, E. D. Siggia, and H. A. Rose, Statistical dynamics of classical systems, *Phys. Rev. A* **8**, 423 (1973).
- [50] H.-K. Janssen, On a Lagrangean for classical field dynamics and renormalization group calculations of dynamical critical properties, *Z. Phys. B* **23**, 377 (1976).
- [51] C. de Dominicis, Techniques de renormalisation de la théorie des champs et dynamique des phénomènes critiques, *J. Phys. (Paris) Colloq.* **37**, 247 (1976).
- [52] L. Canet, B. Delamotte, and N. Wschebor, Fully developed isotropic turbulence: Symmetries and exact identities, *Phys. Rev. E* **91**, 053004 (2015).
- [53] H. Tennekes, Eulerian and Lagrangian time microscales in isotropic turbulence, *J. Fluid Mech.* **67**, 561 (1975).
- [54] J.-B. Lagaert, G. Balarac, and G.-H. Cottet, Hybrid spectral-particle method for the turbulent transport of a passive scalar, *J. Comp. Phys.* **260**, 127 (2014).
- [55] G. Falkovich, Bottleneck phenomenon in developed turbulence, *Phys. Fluids* **6**, 1411 (1994).
- [56] D. A. Donzis and K. R. Sreenivasan, The bottleneck effect and the Kolmogorov constant in isotropic turbulence, *J. Fluid Mech.* **657**, 171 (2010).
- [57] N. V. Antonov, N. M. Gulitskiy, M. M. Kostenko, and A. V. Malyshev, Statistical symmetry restoration in fully developed turbulence: Renormalization group analysis of two models, *Phys. Rev. E* **97**, 033101 (2018).
- [58] D. Squizzato and L. Canet, Kardar-Parisi-Zhang equation with temporally correlated noise: A nonperturbative renormalization group approach, *Phys. Rev. E* **100**, 062143 (2019).